Room temperature coherent control of a single solid-state spin under anti-Stokes excitation

Wu-Xi Lin,[1,3,4,*] Jun-Feng Wang,[2,*] Qiang Li,[1,3,5] Ji-Yang Zhou,[1,3] Zhen-Xuan He,[1,3] Zhi-He Hao,[1,3] Hao Li,[6] Li-Xing You,[6] Jin-Shi Xu,[1,3,4,†] Chuan-Feng Li,[1,3,4,‡] and Guang-Can Guo[1,3,4]

[1]*CAS Key Laboratory of Quantum Information, University of Science and Technology of China, Hefei 230026, China*
[2]*College of Physics, Sichuan University, Chengdu, Sichuan 610065, China*
[3]*CAS Center for Excellence in Quantum Information and Quantum Physics, University of Science and Technology of China, Hefei 230026, China*
[4]*Hefei National Laboratory, University of Science and Technology of China, Hefei 230088, China*
[5]*Institute of Advanced Semiconductors and Zhejiang Provincial Key Laboratory of Power Semiconductor Materials and Devices, ZJU-Hangzhou Global Scientific and Technological Innovation Center, Hangzhou, Zhejiang 311200, China*
[6]*State Key Laboratory of Functional Materials for Informatics, Shanghai Institute of Microsystem and Information Technology, Chinese Academy of Sciences, Shanghai 200050, China*

(Received 12 March 2023; revised 23 November 2023; accepted 4 December 2023; published 26 December 2023)

Single-spin qubits in solid-state materials are important fundamental platforms for quantum information applications. Traditionally, coherent control of solid-state defects is realized under Stokes excitation. Little is known about the coherent control of a single defect spin under anti-Stokes excitation. In this work, we experimentally verify that the mechanism of anti-Stokes excitation of the divacancy in silicon carbide is a phonon-assisted single-photon absorption process and provide the confocal microscopy anti-Stokes photoluminescence scanning image of an isolated single divacancy. Moreover, the optically detected magnetic resonance measurement and coherent control of the single divacancy spin under anti-Stokes excitation are realized at room temperature. We further reveal that the spin readout contrast under anti-Stokes excitation is more robust than that under Stokes excitation at elevated temperatures. Our work establishes a nontraditional protocol for the optical addressing and coherent control of single-spin qubits and expands the boundary of quantum information technology.

DOI: 10.1103/PhysRevB.108.235312

I. INTRODUCTION

Isolated single solid-state defects have aroused great research enthusiasm and have been explored in many works as preeminent candidates for single-photon sources [1–3] and spin qubits [4] applied to quantum computers [5], quantum registers [6], the establishment of light-matter quantum interfaces [7], and quantum sensing with high space resolution and sensitivity [8,9]. However, in most of the previous works, the optical readout and coherent control of single solid-state spin qubits are based on the optically detected magnetic resonance (ODMR) under Stokes excitation with the excitation wavelength shorter than the zero-phonon-line (ZPL) of the defects. Very little is known about the readout and coherent control of single solid-state spin qubits under anti-Stokes excitation, which means that the excitation wavelength is longer than the ZPL. Exploring more types of single-spin readout protocols and coherent control methods is significant to extend the scope of single-spin-qubit-based quantum technologies.

Anti-Stokes emission is a fundamental physical phenomenon [10] that has been observed in various matter systems [11–16]. In recent years, anti-Stokes excitation of solid-state defects has also attracted research enthusiasm, and to date, anti-Stokes-excited photoluminescence (PL) emitted from the defects in hexagonal boron nitride [17], diamond [18–20], and silicon carbide (SiC) [21] has been observed, which can be used for all-optical thermometry [19] and manipulation of the defect charge states [22]. Furthermore, readout and coherent control of spin states under anti-Stokes excitation have also been realized for the silicon vacancy (V_{Si}) ensemble in 4*H*-SiC [21], extending the scope of spin signal readout methods. However, the cornerstone of quantum information is based on the single spin qubit. Moreover, ensemble experiments may sometimes introduce strong background signals from impurities [23]. To build a new protocol for readout and manipulation of single solid-state spin qubits, and further enrich the fundamental physics research on defect spin properties, the ODMR measurement and coherent control of a single solid-state spin must be realized. Unfortunately, due to the intrinsic inefficiency of anti-Stokes PL emission, coherent control of single spin qubits under anti-Stokes excitation remains an arduous task.

In this work, we realize the ODMR readout and coherent control of a single PL6 divacancy spin in 4*H*-SiC under anti-Stokes excitation at room temperature. We first experimentally verify that the mechanism of anti-Stokes excitation of the divacancy is a single-photon absorption process with the assistance of phonons. Then we obtain the confocal PL scanning image of a single PL6 divacancy under anti-Stokes

*These authors contributed equally to this work.
†jsxu@ustc.edu.cn
‡cfli@ustc.edu.cn

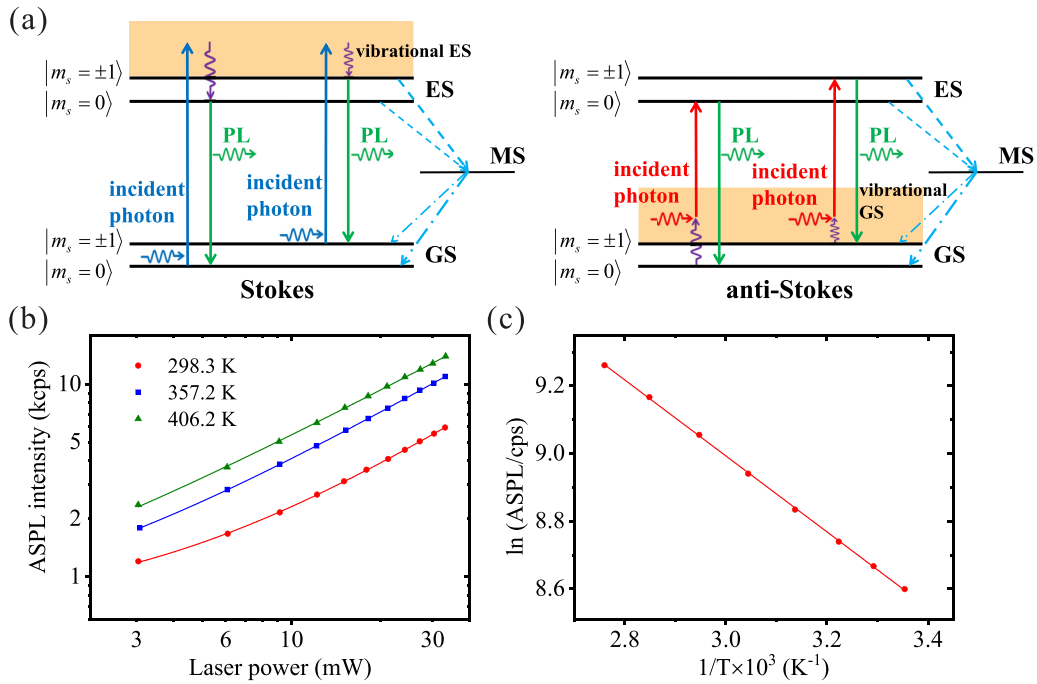

FIG. 1. Energy level diagrams of Stokes and anti-Stokes excitation processes and optical properties of anti-Stokes PL (ASPL) of the divacancy. (a) The processes of Stokes (left) and anti-Stokes (right) excitation. Purple waves represent the absorption and emission of phonons. GS, ES, and MS represent the ground state, the excited state, and the series of metastable states, respectively. (b) The relationship between the anti-Stokes PL intensity and the excitation laser power at three different temperatures. Both the abscissa and longitudinal axes are logarithmic scales. (c) The relationship between the anti-Stokes PL intensity and the temperature under the excitation of a 30 mW 1122 nm laser. The longitudinal axis represents the logarithm of the anti-Stokes PL intensity whose unit is cps, while the abscissa axis represents the reciprocal of the temperature. Here "cps" means "counts per second" and "kcps" means "kilo cps."

excitation, demonstrating the feasibility of the anti-Stokes optical addressing of a single divacancy spin qubit. After that, the ODMR measurement and the coherent control of the single PL6 divacancy spin under anti-Stokes excitation are performed at room temperature. This work paves the way for the use of anti-Stokes methods in single-qubit-based quantum information technologies. Finally, we reveal a potential advantage of anti-Stokes excitation at elevated temperatures.

II. RESULTS

SiC is a kind of wide band-gap semiconductor widely used in high-power electronic devices [24] and optoelectronic devices [25]. There exist several types of defect spin qubits in SiC, such as divacancy [26], V_{Si} [27], and N_CV_{Si} centers [28,29], and they have attracted much attention in quantum technologies. In particular, the divacancy has been widely used in quantum sensing [30,31] and shows great potential for applications in quantum information processing [32] due to its infrared fluorescence [26] and long coherence time even at room temperature [4,32,33]. Several types of divacancy have been discovered, marked as PL1-PL8 [34,35]. Among them, the PL6 divacancy in the crystal stack faults has bright PL intensity and a high ODMR contrast at room temperature [36], thus in the following experiments, we focus on the PL6 divacancy (ZPL at 1038 nm [34,36]). A 1122 nm laser and a 914 nm laser are used for anti-Stokes and Stokes excitation, respectively.

The anti-Stokes excitation processes in various kinds of physical systems can mainly be attributed to three mechanisms, which are multiphoton absorption [11,37,38], Auger recombination [39–41], and phonon assistance [17–19,21,42,43]. For the anti-Stokes excitation process of solid-state defects, the mechanism has been clarified to be a single-photon absorption phonon-assisted process in previous works [17–19,21]. On this basis, a model is utilized to describe the anti-Stokes excitation and PL emission process of the divacancy, which is sketched in Fig. 1(a). For comparison, the Stokes excitation and PL emission process is also provided. Due to the coupling to phonons, the ground state (GS) and excited state (ES) are a set of quasicontinuous vibrational states [44], which are represented by brown shadows. The spin quantum number of the divacancy is $S = 1$ [45], leading to three spin manifolds $|m_s = 0\rangle$ and $|m_s = \pm 1\rangle$ for both the GS and ES.

In the conventional Stokes excitation process, the divacancy at GS is excited by one Stokes photon into one of the vibrational ES and then relaxes to the lowest ES through a phonon relaxation process. After that, the divacancy can directly decay to GS through the spin-preserving radiative transition and emit a PL photon, or through the nonradiative transition that occurs via the mediate metastable state (MS). While for the anti-Stokes excitation process, due to coupling to phonons, the divacancy has a probability of jumping to one of the vibrational GS. With the assistance of the phonon energy, the photon with energy smaller than the energy corresponding to the ZPL can still excite the divacancy into ES.

After that, the divacancy still decays to GS through the radiative or nonradiative transitions, similar to that under Stokes excitation.

To experimentally verify the mechanism of anti-Stokes excitation of the divacancy, we investigate the properties of the anti-Stokes PL of a divacancy ensemble, which is contained in a 4H-SiC sample implanted with an ion fluence (see Appendix A).

For the purpose of demonstrating that anti-Stokes excitation of the divacancy is a single-photon absorption process, we measure the anti-Stokes PL intensity as a function of the excitation laser power. In Fig. 1(b), we show the anti-Stokes PL intensity as a function of the excitation laser power at three different temperatures. The anti-Stokes PL intensity can be fitted by the function $cP^n + d$ (c is the scale factor, P is the excitation laser power, and d is the constant term representing the background signal) [21]. For a single-photon absorption process, the power exponent n is close to 1, while for a multiphoton absorption process, n is obviously larger than 1 [17–19,21]. At 298.3 K, n is fitted to be 0.99 ± 0.01, and at 357.2 K and 406.2 K, n is fitted to be 0.90 ± 0.01 and 0.83 ± 0.01, respectively. All three fitted values of n are close to 1, which strongly proves that anti-Stokes excitation of the divacancy in 4H-SiC is a single-photon absorption process. In Appendix C, the Stokes PL intensity as a function of the excitation power is also provided, demonstrating that the efficiency of anti-Stokes excitation is around 3% that of Stokes excitation at room temperature.

Since anti-Stokes excitation occurs with the assistance of phonons whose energy can fill the energy insufficiency of the excitation photon, the anti-Stokes PL intensity should be proportional to the phonon number density obeying the Bose-Einstein distribution, which can be described as $I_{\mathrm{ASPL}} \propto \{\exp[\Delta E/(k_B T)] - 1\}^{-1}$ [17,18], where ΔE is the gap between the energy of the 1122-nm excitation photon and the ZPL at 1038 nm for PL6, which can be calculated to be 89 meV, and k_B is the Boltzmann constant. Since ΔE is obviously larger than the thermal energy $k_B T$ (around 26 meV at near room temperature), we approximately have $I_{\mathrm{ASPL}} \propto \{\exp[\Delta E/(k_B T)]\}^{-1}$ and thus $\ln I_{\mathrm{ASPL}}$ has an approximately linear relationship with $1/T$ [17,19]. As presented in Fig. 1(c), we measure the anti-Stokes PL intensity of the divacancy as a function of temperature under the excitation of a 30 mW 1122 nm laser and plot the $\ln I_{\mathrm{ASPL}}$-$1/T$ curve. The approximately linear relationship between $\ln I_{\mathrm{ASPL}}$ and $1/T$ proves that anti-Stokes excitation of the divacancy is indeed a phonon-assisted process. ΔE is fitted to be 96 ± 1 meV, which is close to the calculated ΔE (89 meV). In Fig. 1(b), the power index n decreases slowly as temperature increases, and this can be attributed to the decrease of of the phonon assistance efficiency for the photon absorption process as temperature increases [21].

Before the spin manipulation experiment, we need to first optically address an isolated single divacancy spin qubit that is contained in another 4H-SiC sample implanted with a smaller ion fluence (see Appendix A). In Fig. 2(a), we display the confocal PL scanning image of a single PL6 divacancy under Stokes excitation (914 nm, 250 μW) at room temperature. Measurement of the second-order intensity correlation function $g^2(\tau)$ [46] (shown in Appendix E) confirms that this detected isolated PL6 divacancy is a single defect. In Fig. 2(b), we show the confocal PL scanning image of this single PL6 under anti-Stokes excitation (1122 nm, 250 μW) at room temperature. Since the anti-Stokes PL of a single divacancy is very weak, the shown PL scanning image is accumulated by single scanning results to eliminate the background noise and then we take an average. This result demonstrates the feasibility of optically addressing a single divacancy spin qubit under anti-Stokes excitation. By comparing the PL scanning images shown in Figs. 2(a) and 2(b), it can be found that under the same excitation laser power, the PL intensity of the single PL6 under anti-Stokes excitation is approximately 3% that under Stokes excitation at room temperature.

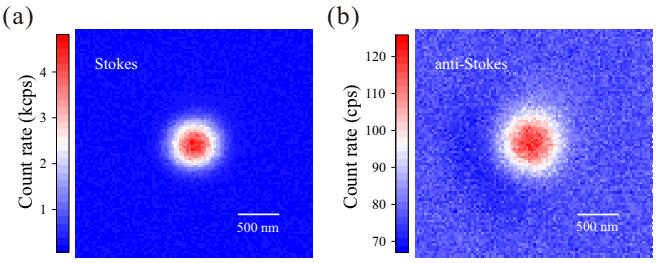

FIG. 2. Confocal PL scanning images of a single PL6 divacancy at room temperature. (a) Confocal PL scanning image under Stokes excitation (914 nm, 250 μW). (b) Confocal PL scanning image under anti-Stokes excitation (1122 nm, 250 μW).

We then turn to the coherent control of this single PL6 divacancy spin under anti-Stokes excitation. The ground state Hamiltonian of divacancy reads $H = D[S_z^2 - \frac{1}{3}S(S+1)] + E(S_x^2 - S_y^2) + g\mu_B \boldsymbol{B} \cdot \boldsymbol{S}$ [35], where D and E are zero-field-splitting (ZFS) parameters, g is the Lande-g factor, μ_B is the Bohr magneton, and $\boldsymbol{B}$ is the external magnetic field. For PL6, $D \approx 1353$ MHz at room temperature and $E \approx 0$ [36], then according to this Hamiltonian, $|m_s = \pm 1\rangle$ are degenerate without the external magnetic field, so we use a magnetic field perpendicular to the sample surface, which is also along the spin orientation of PL6, to split $|m_s = \pm 1\rangle$. The two energy gaps corresponding to transitions $|m_s = 0\rangle \leftrightarrow |m_s = \pm 1\rangle$ can be calculated to be $D \pm g\mu_B B$ from the Hamiltonian, and can be experimentally fitted from the ODMR spectrum. The spin qubit coherently controlled in this work consists of $|m_s = 0\rangle$ and $|m_s = -1\rangle$ corresponding to the resonant frequency of the left branch of the ODMR spectrum. The principles of optical spin polarization and readout in the ODMR measurement and coherent control under anti-Stokes and Stokes excitation are both explained in Appendix F.

Here, we perform the coherent control of this single PL6 divacancy spin under anti-Stokes excitation at room temperature in a 3.4 mT external magnetic field. For comparison, the results under Stokes excitation are also exhibited. In Figs. 3(a) and 3(b), the left and right branches of the ODMR spectra of the single PL6 spin under anti-Stokes and Stokes excitation are displayed. It can be found that the resonant frequencies f_{res1} and f_{res2} of the single PL6 divacancy spin remain the same under anti-Stokes and Stokes excitation, which signifies an unchanged spin state structure under anti-Stokes and Stokes excitation at the level of a single divacancy spin. The slight difference between ODMR contrasts under anti-Stokes

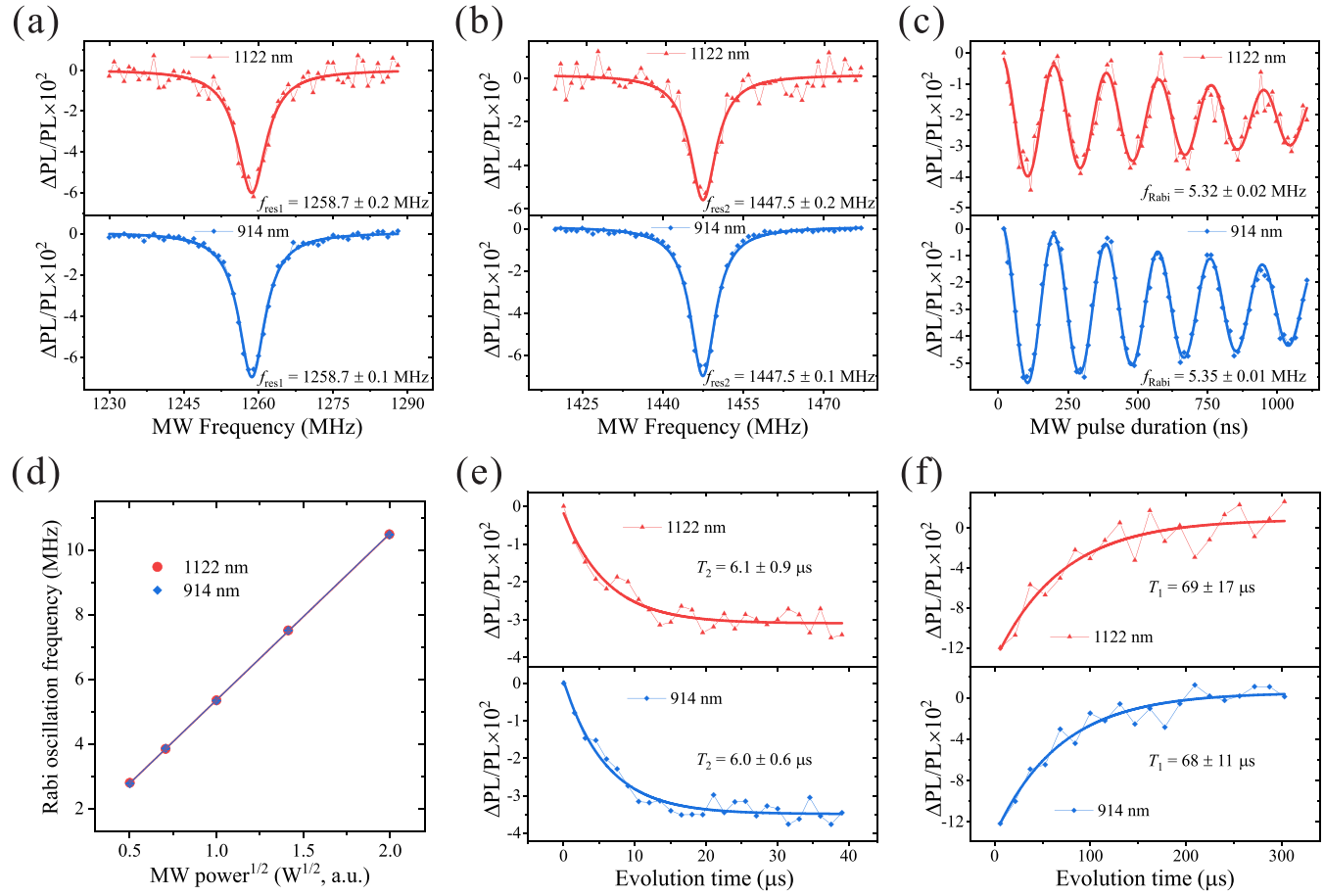

FIG. 3. Coherent control of a single PL6 divacancy spin in a 3.4 mT magnetic field under anti-Stokes (1122 nm) and Stokes (914 nm) excitation at room temperature. The upper column and bottom column represent the cases under anti-Stokes and Stokes excitation, respectively. (a) and (b) Left and right branches of the ODMR spectra. f_{res1} and f_{res2} are the two resonant frequencies. (c) Rabi oscillations driven by the same MW power. f_{Rabi} represents the Rabi oscillation frequency. (d) The relationship between the Rabi oscillation frequencies and the MW power under anti-Stokes (red circles) and Stokes (blue rhombuses) excitation. The abscissa axis represents the normalized square root of the MW power. Standard deviations are smaller than the size of data dots. (e) Spin echo curves. T_2 is the coherence time fitted from the spin echo curve. (f) Depolarization curves. T_1 is the longitudinal spin relaxation time fitted from the depolarization curve.

and Stokes excitation can be attributed to the influence from the background signal. As shown in Fig. 2, the anti-Stokes PL intensity of the single PL6 is around only 3% that under Stokes excitation, so the background signal has a larger effect on the ODMR contrast under anti-Stokes excitation.

In the coherent control experiment of the single PL6 spin, we fix the microwave (MW) frequency at f_{res1}. Figure 3(c) shows the Rabi oscillation curves of the single PL6 spin under anti-Stokes and Stokes excitation driven by the same MW power. The Rabi oscillation frequencies f_{Rabi} under anti-Stokes and Stokes excitation are very close. In Fig. 3(d), we show the relationship between the Rabi oscillation frequency of the single PL6 spin and the MW power under anti-Stokes and Stokes excitation. This figure demonstrates that under both anti-Stokes and Stokes excitation, the Rabi oscillation frequencies of the single PL6 spin have an accurate proportional relationship with the square root of the MW power.

In Fig. 3(e), we show the spin echo curves of the single PL6 under anti-Stokes and Stokes excitation. The coherence times T_2 fitted from spin echo curves under anti-Stokes and Stokes excitation are both approximately 6 μs, which are very close. As presented in Fig. 3(f), we measure the depolarization curves of the single PL6 spin under anti-Stokes and Stokes excitation. The longitudinal spin relaxation times T_1 fitted from depolarization curves under anti-Stokes and Stokes excitation are also very close. Both T_2 and T_1 of a single PL6 spin are almost the same under anti-Stokes and Stokes excitation, which can prove that the coherent properties of a single divacancy spin do not change under anti-Stokes excitation compared with those under traditional Stokes excitation.

We also realize the coherent control of the PL6 divacancy ensemble spins under anti-Stokes excitation at room temperature, and the results are displayed in Appendix D. Meanwhile, we also compare the ODMR contrasts of the PL6 ensemble spins under anti-Stokes and Stokes excitation at elevated temperatures. In Figs. 4(a) and 4(b), we show the left branches of the ODMR spectra of the PL6 ensemble spins under anti-Stokes and Stokes excitation at different temperatures. Figure 4(c) shows the temperature dependences of the ODMR contrasts under anti-Stokes and Stokes excitation. As demonstrated by these results, when the temperature increases to be higher than room temperature, the ODMR contrast under

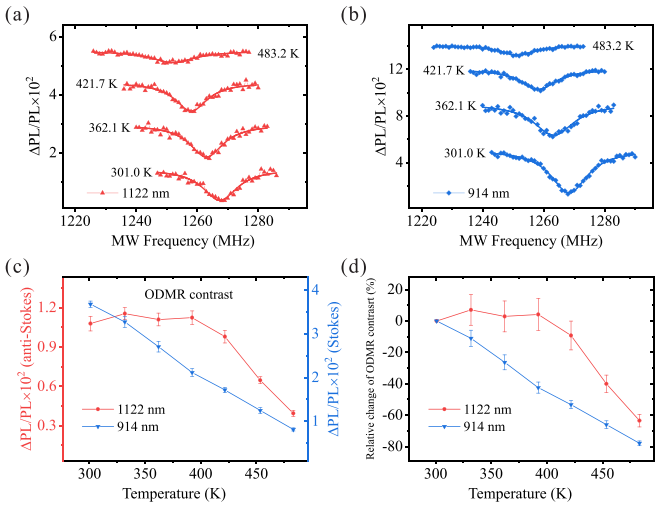

FIG. 4. Temperature dependences of the ODMR contrasts of the PL6 ensemble spins under anti-Stokes (1122 nm) and Stokes (914 nm) excitation at room temperature and higher temperatures. (a) and (b) The left branches of the ODMR spectra in a 3.0 mT magnetic field under anti-Stokes and Stokes excitation, respectively, at different temperatures. (c) Temperature dependences of the ODMR contrasts under anti-Stokes and Stokes excitation. (d) Relative changes of the ODMR contrasts at higher temperatures compared with the ODMR contrasts at room temperature under anti-Stokes and Stokes excitation.

anti-Stokes excitation remains almost the same below around 400 K, while under the conventional Stokes excitation, the ODMR contrast decreases apparently as the temperature increases. In Fig. 4(d), we display the relative changes of the ODMR contrasts at higher temperatures compared with the ODMR contrasts at room temperature under anti-Stokes and Stokes excitation. This figure shows that from room temperature to around 480 K, the relative decrease of the ODMR contrast under anti-Stokes excitation is smaller than that under Stokes excitation. These results demonstrate a more robust ODMR measurement operation under anti-Stokes excitation than that under Stokes excitation at elevated temperatures. The mechanism of this phenomenon may be that since anti-Stokes excitation itself is a phonon-assisted process, the adverse effect of the phonon perturbation, which causes the ODMR contrast to decrease as the temperature increases, can be partly offset under anti-Stokes excitation. Here, we only investigate the temperature dependence of the ODMR contrast of the PL6 ensemble spins instead of a single PL6 spin because a single PL6 can only be optically addressed by using an objective with a large numerical aperture (NA) (see Appendix A), which induces a small distance between the objective and the sample surface and then can cause the objective to be harmed by the high temperature as the temperature increases. In the future, the use of a microstructure such as a solid immersion lens [47], a nanopillar [48], or a circular bullseye grating [49] can increase the PL collection efficiency and make the optical addressing of a single divacancy by using an objective with a smaller NA possible, leading to the overcoming of this obstacle.

III. CONCLUSIONS

In conclusion, we realize the ODMR measurement and coherent control of a single PL6 divacancy spin under anti-Stokes excitation. We first experimentally verify that anti-Stokes excitation of the divacancy in 4*H*-SiC is a phonon-assisted single-photon absorption process by measuring the intensity of the anti-Stokes PL from a divacancy ensemble as functions of the excitation laser power and temperature. Then, we provide the confocal anti-Stokes PL scanning image of a single PL6 divacancy. After that, we realize the ODMR measurement and coherent control of this single PL6 divacancy spin under anti-Stokes excitation at room temperature. The ODMR spectra, Rabi oscillation frequencies, coherence times T_2, and longitudinal spin relaxation times T_1 of this single PL6 spin are all very close under anti-Stokes and Stokes excitation. This fact demonstrates that the spin state structure and coherent properties do not change under anti-Stokes excitation compared with those under Stokes excitation at the level of a single divacancy spin qubit. This work constructs the basis of coherently manipulating a single spin qubit under anti-Stokes excitation. It contributes to establishing an unconventional protocol for the addressing, readout, and coherent control of single-spin qubits, and makes progress in the fundamental spin physics by deepening the understanding of the properties of a single solid-state defect spin. We also demonstrate that the ODMR measurement operation is more robust under anti-Stokes excitation than that under Stokes excitation at elevated temperatures. Anti-Stokes excitation can also have the advantage over Stokes excitation for solid-state-spin-based quantum sensing inside living cells [50] due to the relatively minor phototoxicity [51,52] and the more negligible photon scattering effect [53] leading to a larger penetration depth inside living cells [54] of the relatively longer excitation wavelength.

ACKNOWLEDGMENTS

We thank F.-F. Yan for the helpful discussion. This work was supported by the Innovation Program for Quantum Science and Technology (Grant No. 2021ZD0301400), the National Natural Science Foundation of China (Grants No. U19A2075, No. 92365205, No. 61725504, No. 11821404, No. 61905233, and No. 11975221), the Anhui Initiative in Quantum Information Technologies (Grant No. AHY060300), the Fundamental Research Funds for the Central Universities (Grant No. WK2470000026), and the National Postdoctoral Program for Innovative Talents (Grant No. BX20200326). This work was partially performed at the University of Science and Technology of China Center for Micro and Nanoscale Research and Fabrication.

APPENDIX A: EXPERIMENTAL SETUP

The samples used in our work are both sliced from a high-purity epitaxial 4*H*-SiC wafer. For the sample containing isolated single divacancies, we use a $5\times10^{11}/\mathrm{cm}^2$ carbon ion (C^+) fluence with an ion kinetic energy of 30 keV to implant it. While the divacancy ensemble sample is implanted by a $1\times10^{14}/\mathrm{cm}^2$ fluence of nitrogen molecule ion (N_2^+) with an ion kinetic energy of 30 keV. After implantation, both samples are annealed at 900 °C for 30 minutes.

In this work, a homebuilt confocal microscopy system is used for the excitation of the divacancy. A 1122 nm laser and a 914 nm laser are used for anti-Stokes and Stokes excitation, respectively. For verification of the mechanism of anti-Stokes excitation shown in Fig. 1 of the main text, the measurement of the temperature dependences of the ODMR contrasts under anti-Stokes and Stokes excitation for PL6 ensemble spins shown in Fig. 4 of the main text, and the comparison of the anti-Stokes and Stokes excitation efficiencies shown in Fig. 6 of Appendix C, we use an air objective with NA = 0.65 to focus the laser and collect PL, while in all the other experiments, the objective used is an oil immersion objective with NA = 1.30. The PL collected is filtered by a bandpass filter whose passband is 1020-1090 nm (Semrock) and a 1100-nm short-pass filter (Edmund Optics). Besides filtering out the excitation laser, the filters can also exclude the influence of the PL emitted from the N_CV_{Si} centers in the defect ensemble whose ZPLs are longer than 1150 nm [28] and can be Stokes excited by the 1122 nm laser. And then the filtered PL is coupled into the fiber and sent to a superconducting nanowire single photon detector (SNSPD, Photech). Count signals from the SNSPD are recorded by a data acquisition (DAQ) device (National Instruments). The laser and microwave (MW) pulse sequences used for the coherent control are generated by an acousto-optic modulator (AOM) and an MW switch, respectively. The electrical pulse signals used to control the AOM and MW switch, as well as trigger the record function of the DAQ device, are generated by a pulse blaster board (PBESR-PRO-500, SpinCore). The ODMR measurement and coherent control results are displayed by the relative variation of the PL intensity $\Delta PL/PL$. The devices used for the temperature control of the sample are a metal ceramic heater (HT24S, Thorlabs) for heating the sample and a resistive temperature detector (TH100PT, Thorlabs) for real-time monitoring of the sample temperature. The measurement of $g^2(\tau)$ is realized by a time-to-digital converter (id800, IDQ), which can record the delay time τ between two PL photon paths.

APPENDIX B: ANTI-STOKES AND STOKES PL SPECTRA OF THE DIVACANCY ENSEMBLE

In Fig. 5, the PL spectra of the divacancy ensemble at room temperature under anti-Stokes and Stokes excitation are displayed. The PL spectrum envelope under anti-Stokes excitation has a small redshift compared with that under Stokes excitation, which has also been observed for the V_{Si} ensemble in 4*H*-SiC [21]. The normalization factor of the Stokes PL spectrum is approximately 30.5 times that of the anti-Stokes PL spectrum, which indicates the Stokes to anti-Stokes PL intensity ratio of the divacancy ensemble.

APPENDIX C: COMPARISON OF THE EXCITATION EFFICIENCY BETWEEN ANTI-STOKES AND STOKES EXCITATION

In order to compare the excitation efficiency between anti-Stokes excitation and Stokes excitation, in Fig. 6(a), we show the dependences of the PL intensities of the divacancy ensemble under anti-Stokes and Stokes excitation on the excitation laser power at room temperature. The ratios of the PL intensities under anti-Stokes excitation to those under Stokes excitation with the same excitation laser powers can be derived from the data shown in Fig. 6(a), which are displayed in Fig. 6(b). From the result shown in this figure, it can be demonstrated that under the same excitation laser power, the anti-Stokes PL intensity is around 3% of the Stokes PL intensity at room temperature, which conforms to the PL ratio displayed by the PL spectra shown in Fig. 5.

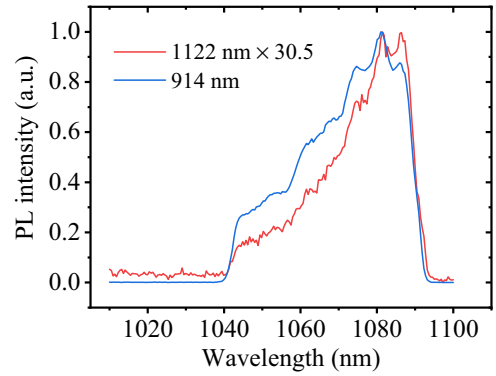

FIG. 5. PL spectra of the divacancy ensemble under anti-Stokes (1122 nm) and Stokes (914 nm) excitation at room temperature. The labeled coefficient 30.5 is the anti-Stokes PL spectrum magnification time to normalize the data. "a.u." means "arbitrary unit."

APPENDIX D: COHERENT CONTROL OF THE DIVACANCY ENSEMBLE SPINS UNDER ANTI-STOKES AND STOKES EXCITATION

We have operated coherent control of the PL6 divacancy ensemble spins under anti-Stokes and Stokes excitation at room temperature in a 3.0 mT magnetic field. In Fig. 7(a), we show the left branches of the ODMR spectra of the PL6 ensemble spins under anti-Stokes and Stokes excitation. The ODMR resonant frequencies f_{res} of the PL6 ensemble spins under anti-Stokes and Stokes excitation are very close. In the coherent control, we set the MW frequency to f_{res}. As presented in Fig. 7(b), Rabi oscillations of the PL6 ensem-

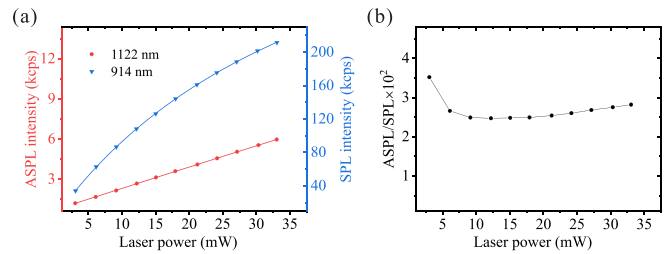

FIG. 6. Comparison of the anti-Stokes and Stokes excitation efficiencies. (a) The PL intensities of the divacancy ensemble under anti-Stokes and Stokes excitation as functions of the excitation laser power at room temperature. (b) The ratios of the PL intensities under anti-Stokes excitation to those under Stokes excitation with the same excitation laser powers derived from (a). The result shown in this figure demonstrates that the anti-Stokes excitation efficiency is approximately 3% of the Stokes excitation efficiency at room temperature.

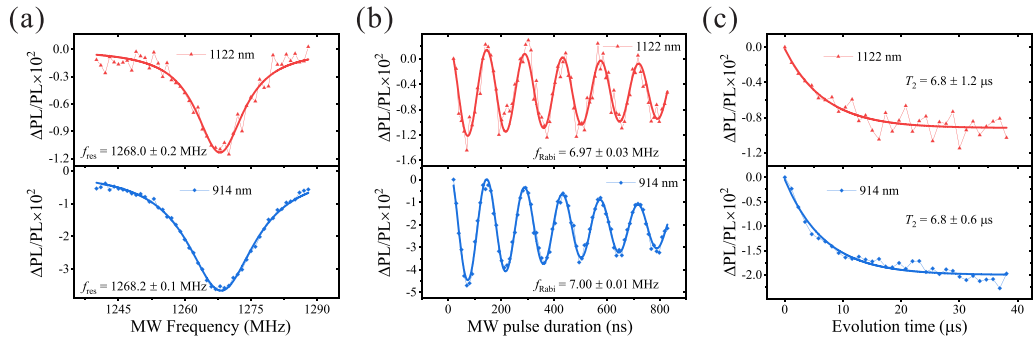

FIG. 7. Coherent control of the PL6 divacancy ensemble spins in a 3.0 mT magnetic field under anti-Stokes and Stokes excitation at room temperature. The upper column and bottom column represent the cases under anti-Stokes and Stokes excitation, respectively. (a) The left branches of the ODMR spectra. $f_{\rm res}$ represents the resonant frequency. (b) Rabi oscillations driven by the same MW power. $f_{\rm Rabi}$ represents the Rabi oscillation frequency. (c) Spin echo curves. T_2 is the coherence time fitted from the spin echo curve.

ble spins under anti-Stokes and Stokes excitation are driven by MW with the same power, and the Rabi oscillation frequencies $f_{\rm Rabi}$ are very close to each other under anti-Stokes and Stokes excitation for the PL6 ensemble spins. The spin echo curves of the PL6 ensemble spins under anti-Stokes and Stokes excitation are shown in Fig. 7(c). The coherence times T_2 fitted from the spin echo curves are both 6.8 μs under anti-Stokes and Stokes excitation for the PL6 ensemble spins. These experimental results demonstrate that the coherent properties of spins remain the same under anti-Stokes and Stokes excitation for the divacancy ensemble.

APPENDIX E: CONFIRMATION OF THE DETECTED ISOLATED PL6 DIVACANCY AS A SINGLE DEFECT

To confirm that the detected isolated PL6 divacancy shown in Fig. 2 of the main text is a single defect, we measure the second-order intensity correlation function $g^2(\tau)$ [46], and the result is shown in Fig. 8. The experimental data are fitted by the function $g^2(\tau) = 1 - (1 + a)e^{-|\tau|/\tau_1} + be^{-|\tau|/\tau_2}$, where a, b, τ_1, and τ_2 are fitting parameters [28,36]. Because $g^2(0)$ is much smaller than 0.5, the detected PL6 divacancy is indeed a single defect.

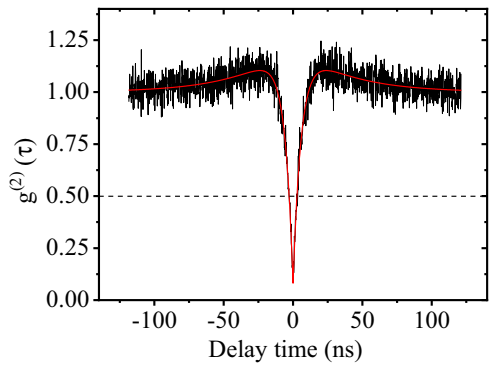

FIG. 8. Measurement of the second-order intensity correlation function $g^2(\tau)$ for the detected isolated PL6 divacancy. The black line shows the experimental data, and the red line is the fitting line. The dashed line is the bound of 0.5. $g^2(0) < 0.5$ verifies the single-photon emission.

APPENDIX F: PRINCIPLES OF OPTICAL POLARIZATION AND READOUT OF THE DIVACANCY SPIN STATE UNDER STOKES AND ANTI-STOKES EXCITATION

In the operation of the ODMR measurement and coherent control of the divacancy spins under both Stokes and anti-Stokes excitation, the optical polarization by laser pumping and the readout of the spin state by detecting the variation of PL intensity are crucial. Here, we establish a simple five-level model to explain the mechanism of the optical polarization and the readout of the divacancy spin state in both Stokes and anti-Stokes excitation processes, which are sketched in Fig. 9.

In this figure, we have marked the decay rates between the ground state (GS), the excited state (ES), and the mediate metastable state (MS), while the excitation rates under Stokes and anti-Stokes excitation are also marked. In both Stokes and anti-Stokes excitations, the absorption and emission of phonons are spin-conserving [21], and the radiative transitions are also spin-preserving [21], so the operators corresponding to both of these processes should be spin-independent. Due to this, the excitation rates and the decay rates of radiative transitions for both $|m_s = 0\rangle$ and $|m_s = \pm 1\rangle$ should be the same. For both $|m_s = 0\rangle$ and $|m_s = \pm 1\rangle$, under Stokes and anti-Stokes excitation, the excitation rates are marked as $c_{\rm S}$ and $c_{\rm AS}$ respectively, and under both Stokes and anti-Stokes excitation, the decay rate directly from ES to GS in the radiative transition is marked as r_{eg}. The nonradiative transition via MS, which is also called intersystem crossing (ISC), is spin-dependent. For $|m_s = 0\rangle$, the decay rate from ES to MS is marked as $r_{em,0}$ and that from MS to GS is marked as $r_{mg,0}$, while for $|m_s = \pm 1\rangle$, the decay rate from ES to MS is marked as $r_{em,1}$ and that from MS to GS is marked as $r_{mg,1}$. The divacancy populations at the corresponding states, which mean the probabilities of the divacancy being at the corresponding states, are also marked in Fig. 9. The GS populations at $|m_s = 0\rangle$ and $|m_s = \pm 1\rangle$ are marked as n_{g0} and n_{g1}, respectively, while the ES populations at $|m_s = 0\rangle$ and $|m_s = \pm 1\rangle$ are marked as n_{e0} and n_{e1}, respectively. The MS population is marked as n_m.

Then, we can establish a set of equations to describe the change of these populations with time as follows. For Stokes

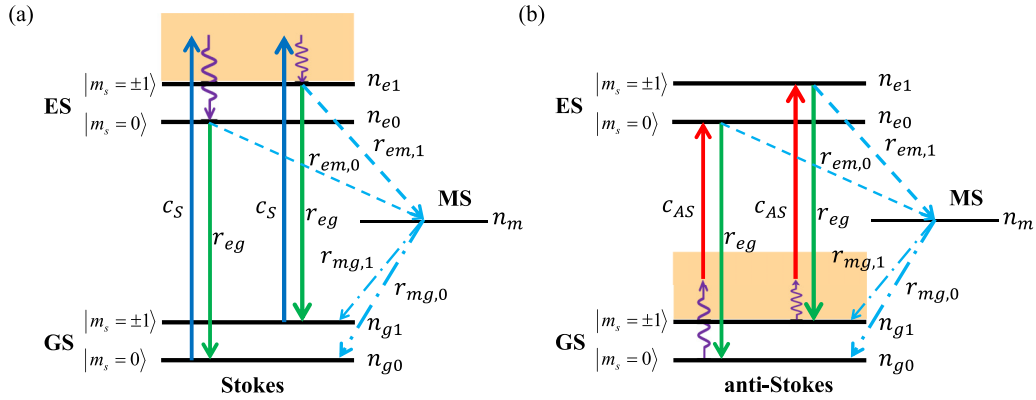

FIG. 9. A simple five-level model describing the mechanism of the optical polarization and the readout of the divacancy spin state. The excitation and decay rates, as well as the divacancy populations at the corresponding states, are marked in this figure. (a) The case under Stokes excitation. (b) The case under anti-Stokes excitation.

excitation, these equations are

$$\begin{aligned}
\frac{dn_{g0}}{dt} &= -c_S n_{g0} + r_{eg} n_{e0} + r_{mg,0} n_m \\
\frac{dn_{g1}}{dt} &= -c_S n_{g1} + r_{eg} n_{e1} + r_{mg,1} n_m \\
\frac{dn_{e0}}{dt} &= c_S n_{g0} - r_{eg} n_{e0} - r_{em,0} n_{e0} \\
\frac{dn_{e1}}{dt} &= c_S n_{g1} - r_{eg} n_{e1} - r_{em,1} n_{e1} \\
\frac{dn_m}{dt} &= r_{em,0} n_{e0} + r_{em,1} n_{e1} - r_{mg,0} n_m - r_{mg,1} n_m \\
n_{g0} + n_{g1} + n_{e0} + n_{e1} + n_m &= 1. \qquad \text{(F1)}
\end{aligned}$$

For anti-Stokes excitation, these equations are

$$\begin{aligned}
\frac{dn_{g0}}{dt} &= -c_{AS} n_{g0} + r_{eg} n_{e0} + r_{mg,0} n_m \\
\frac{dn_{g1}}{dt} &= -c_{AS} n_{g1} + r_{eg} n_{e1} + r_{mg,1} n_m \\
\frac{dn_{e0}}{dt} &= c_{AS} n_{g0} - r_{eg} n_{e0} - r_{em,0} n_{e0} \\
\frac{dn_{e1}}{dt} &= c_{AS} n_{g1} - r_{eg} n_{e1} - r_{em,1} n_{e1} \\
\frac{dn_m}{dt} &= r_{em,0} n_{e0} + r_{em,1} n_{e1} - r_{mg,0} n_m - r_{mg,1} n_m \\
n_{g0} + n_{g1} + n_{e0} + n_{e1} + n_m &= 1. \qquad \text{(F2)}
\end{aligned}$$

In the calculation of the spin polarization effect by laser pumping, we only focus on the steady-state solutions of these equations, under which condition $\frac{dn_{g0}}{dt} = \frac{dn_{g1}}{dt} = \frac{dn_{e0}}{dt} = \frac{dn_{e1}}{dt} = \frac{dn_m}{dt} = 0$. Then, the steady populations at GS under Stokes excitation can be solved as

$$n_{g0} = \frac{\left(1 + \frac{r_{eg}}{r_{em,0}}\right)\frac{r_{mg,0}}{c_S}}{1 + \left(1 + \frac{r_{eg}}{c_S}\right)\left(\frac{r_{mg,0}}{r_{em,0}} + \frac{r_{mg,1}}{r_{em,1}}\right) + \frac{r_{mg,0}+r_{mg,1}}{c_S}}, \qquad \text{(F3)}$$

$$n_{g1} = \frac{\left(1 + \frac{r_{eg}}{r_{em,1}}\right)\frac{r_{mg,1}}{c_S}}{1 + \left(1 + \frac{r_{eg}}{c_S}\right)\left(\frac{r_{mg,0}}{r_{em,0}} + \frac{r_{mg,1}}{r_{em,1}}\right) + \frac{r_{mg,0}+r_{mg,1}}{c_S}}. \qquad \text{(F4)}$$

And the steady populations at GS under anti-Stokes excitation can be solved as

$$n_{g0} = \frac{\left(1 + \frac{r_{eg}}{r_{em,0}}\right)\frac{r_{mg,0}}{c_{AS}}}{1 + \left(1 + \frac{r_{eg}}{c_{AS}}\right)\left(\frac{r_{mg,0}}{r_{em,0}} + \frac{r_{mg,1}}{r_{em,1}}\right) + \frac{r_{mg,0}+r_{mg,1}}{c_{AS}}}, \qquad \text{(F5)}$$

$$n_{g1} = \frac{\left(1 + \frac{r_{eg}}{r_{em,1}}\right)\frac{r_{mg,1}}{c_{AS}}}{1 + \left(1 + \frac{r_{eg}}{c_{AS}}\right)\left(\frac{r_{mg,0}}{r_{em,0}} + \frac{r_{mg,1}}{r_{em,1}}\right) + \frac{r_{mg,0}+r_{mg,1}}{c_{AS}}}. \qquad \text{(F6)}$$

From the above solutions, it can be found that under both Stokes and anti-Stokes excitation, we have the same population ratio between n_{g0} and n_{g1} as

$$n_{g0}/n_{g1} = \frac{r_{mg,0}}{r_{mg,1}} \frac{r_{em,1}}{r_{em,0}} \frac{r_{eg} + r_{em,0}}{r_{eg} + r_{em,1}}, \qquad \text{(F7)}$$

which is irrelevant to the excitation rate c_S or c_{AS}. For a defect that is a bright single-photon source, we have $r_{eg} \gg r_{em,0}$ and $r_{eg} \gg r_{em,1}$, then we approximately have

$$n_{g0}/n_{g1} \approx \frac{r_{mg,0}}{r_{mg,1}} \frac{r_{em,1}}{r_{em,0}}. \qquad \text{(F8)}$$

From this result, we find that under both Stokes and anti-Stokes excitation, the fact that the nonradiative decay rates from ES to MS and from MS to GS are different between different spin states is crucial for the effect of optical spin polarization, since if $r_{mg,0} = r_{mg,1}$ and $r_{em,0} = r_{em,1}$, we have $n_{g0}/n_{g1} = 1$ (this relationship still holds for formula (F7) without approximation, so here we use equal sign instead of approximately equal sign) and there will be no spin polarization effect. As a usual definition [21], the spin polarization parameter P is $P = \frac{n_{g0}-n_{g1}}{n_{g0}+n_{g1}} \approx \frac{r_{mg,0}r_{em,1}-r_{mg,1}r_{em,0}}{r_{mg,0}r_{em,1}+r_{mg,1}r_{em,0}}$, which is determined by the nonradiative decay rates. For PL6, the spin state is polarized to $|m_s = 0\rangle$ [55], so there is likely to exist the relationships $r_{mg,0} > r_{mg,1}$ and $r_{em,0} < r_{em,1}$, which correspond to the line thicknesses of the nonradiative decay arrows shown in Fig. 9 (the thicker arrow represents the larger decay rate).

For the readout of the spin state, we focus on the expression of the PL intensity. Since only radiative transitions can emit PL photons, the PL intensity can be expressed by the populations at ES under both Stokes and anti-Stokes

excitation as

$$\mathrm{PL} = N r_{eg}(n_{e0} + n_{e1}). \tag{F9}$$

Here, N is the number of the divacancies that have been excited. For a single divacancy, $N = 1$. Although the steady-state condition cannot be used under this case, since the lifetime of ES is much shorter than those of MS and GS, the populations at ES are always close to 0, so we approximately still have $\frac{dn_{e0}}{dt} \approx 0$, $\frac{dn_{e1}}{dt} \approx 0$, then from the third and fourth equations in formulas (F1) and (F2), we can obtain that under Stokes excitation, $n_{e0} \approx \frac{c_S}{r_{eg}+r_{em,0}} n_{g0}$ and $n_{e1} \approx \frac{c_S}{r_{eg}+r_{em,1}} n_{g1}$, and under anti-Stokes excitation, $n_{e0} \approx \frac{c_{AS}}{r_{eg}+r_{em,0}} n_{g0}$ and $n_{e1} \approx \frac{c_{AS}}{r_{eg}+r_{em,1}} n_{g1}$. Then, the PL intensities under Stokes and anti-Stokes excitation can now be expressed by the GS populations with different spin states as

$$\mathrm{PL(Stokes)} \approx N c_S r_{eg}\left(\frac{n_{g0}}{r_{eg}+r_{em,0}} + \frac{n_{g1}}{r_{eg}+r_{em,1}}\right) \propto c_S, \tag{F10}$$

$$\mathrm{PL(anti\text{-}Stokes)} \approx N c_{AS} r_{eg}\left(\frac{n_{g0}}{r_{eg}+r_{em,0}} + \frac{n_{g1}}{r_{eg}+r_{em,1}}\right) \propto c_{AS}. \tag{F11}$$

c_{AS} is proportional to the number density of the phonons whose energy can fill the energy insufficiency of the excitation photon, which is $\{\exp[\Delta E/(k_B T)] - 1\}^{-1}$ as described in the main text [17,18], and this number density is usually much smaller than 1, thus, there usually exists the relationship $c_{AS} \ll c_S$, which leads the PL intensity under anti-Stokes excitation to be much smaller than that under Stokes excitation [19,21].

In the weak illumination limit which is an approximate condition when the excitation laser power is not too large, the divacancy is most likely to be at the ground state, under this condition $n_{g0} + n_{g1} \approx 1$ [21]. And as described above, for a defect that is a bright single-photon source, we have $r_{eg} \gg r_{em,0}$ and $r_{eg} \gg r_{em,1}$. By using these conditions, we approximately have that under Stokes and anti-Stokes excitation,

$$\begin{aligned}\mathrm{PL(Stokes)} &\approx N c_S\left(1 - \frac{r_{em,1}}{r_{eg}} + \frac{r_{em,1} - r_{em,0}}{r_{eg}} n_{g0}\right) \\ &\approx N c_S\left(1 - \frac{r_{em,0}}{r_{eg}} - \frac{r_{em,1} - r_{em,0}}{r_{eg}} n_{g1}\right),\end{aligned} \tag{F12}$$

$$\begin{aligned}\mathrm{PL(anti\text{-}Stokes)} &\approx N c_{AS}\left(1 - \frac{r_{em,1}}{r_{eg}} + \frac{r_{em,1} - r_{em,0}}{r_{eg}} n_{g0}\right) \\ &\approx N c_{AS}\left(1 - \frac{r_{em,0}}{r_{eg}} - \frac{r_{em,1} - r_{em,0}}{r_{eg}} n_{g1}\right).\end{aligned} \tag{F13}$$

Therefore the variations of PL intensities under Stokes and anti-Stokes excitation can be expressed as

$$\begin{aligned}\Delta\mathrm{PL(Stokes)} &\approx N c_S \frac{r_{em,1} - r_{em,0}}{r_{eg}} \Delta n_{g0} \\ &\approx -N c_S \frac{r_{em,1} - r_{em,0}}{r_{eg}} \Delta n_{g1},\end{aligned} \tag{F14}$$

$$\begin{aligned}\Delta\mathrm{PL(anti\text{-}Stokes)} &\approx N c_{AS} \frac{r_{em,1} - r_{em,0}}{r_{eg}} \Delta n_{g0} \\ &\approx -N c_{AS} \frac{r_{em,1} - r_{em,0}}{r_{eg}} \Delta n_{g1}.\end{aligned} \tag{F15}$$

Thus the variations of both the Stokes and anti-Stokes PL intensities are proportional to the variation of the population at GS with $|m_s = 0\rangle$ or $|m_s = \pm 1\rangle$, so under both Stokes and anti-Stokes excitation, the variation of the PL intensity can be a tool for the readout of the spin state. And it can be discovered that the spin-dependence of the nonradiative decay rates is still crucial for the optical readout of the spin state, since if $r_{em,1} = r_{em,0}$, from formulas (F14) and (F15) it can be found that $\Delta\mathrm{PL} \approx 0$ under both Stokes and anti-Stokes excitation, which cannot reflect the change of the spin state.

From another perspective, as mentioned above, the prerequisite of realizing the optical spin polarization and readout processes in the ODMR measurement and coherent control under anti-Stokes excitation is the spin-conserving property of the phonon absorption process. In fact, this spin-conserving property is not so apparent because at room temperature, the thermal energy is around 26 meV, while the energy splitting between different spin states is the order of magnitude of 10^{-3} meV, which is four orders of magnitude smaller than the thermal energy. It is worth experimentally validating this property. The realization of the ODMR measurement and coherent control of a single divacancy spin under anti-Stokes excitation in our work experimentally proves this spin-conserving property of the phonon absorption process at the level of a single solid-state defect spin, which enriches the fundamental physics research on defect spin properties.

APPENDIX G: LASER AND MW PULSE SEQUENCES USED IN THE COHERENT CONTROL EXPERIMENTS

In the coherent control of the divacancy ensemble spins and the single divacancy spin, we use laser pulses for the optical polarization of spins and the readout of the spin states, and use microwave (MW) pulses for the manipulation of the spin states. We also need to use the trigger pulse generated by the pulse blaster board to enable the record function of the DAQ device used to record the count signals generated by the SNSPD, which is defined as the "detection pulse" here. Figure 10 displays the laser, MW, and detection pulse sequences used for different coherent control operations.

For measurement of the Rabi oscillation, the pulse sequence is displayed in Fig. 10(a); for measurement of the spin echo curve, the pulse sequence is displayed in Fig. 10(b); for measurement of the depolarization curve, the pulse sequence is displayed in Fig. 10(c). In both Figs. 10(b) and 10(c), we use τ to represent the free evolution time of the divacancy spin, and in the main text, the abscissa axes "evolution time" of the spin echo curves and depolarization curves are just the "τ" here. Also in these two figures, $\pi/2$ and π represent the MW pulses whose duration times are 1/4 and 1/2 Rabi oscillation periods, respectively [26]. In the pulse sequences used for the Rabi oscillation and spin echo measurements, the first laser pulse is used for the spin polarization, and the second laser

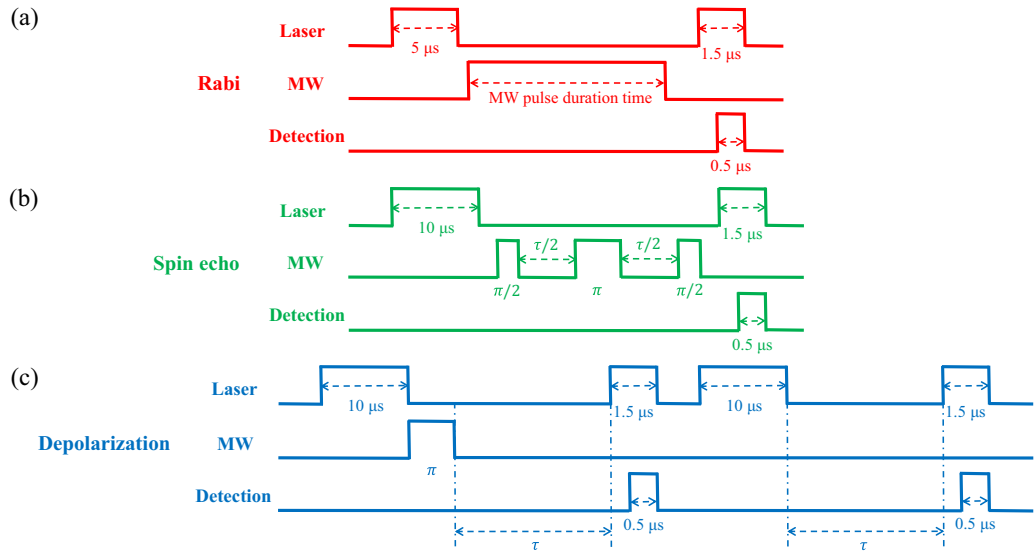

FIG. 10. Laser, microwave, and detection pulse sequences used for the coherent control of the divacancy spin. (a) The pulse sequence used for the Rabi oscillation measurement. (b) The pulse sequence used for the spin echo measurement. (c) The pulse sequence used for the depolarization measurement.

pulse is used for the readout of the spin state; in the pulse sequence used for the depolarization measurement, the first and third laser pulses are used for the spin polarization, and the second and fourth laser pulses are used for the readout of the spin state. The detection pulse is generated by the pulse blaster board after the laser pulse used for readout of the spin state has been exciting the divacancy for 1 μs. In the depolarization measurement, we record the difference between the results corresponding to the first and second detection pulses that measure the PL intensity with and without the action of the MW π pulse respectively, which is the same as the previous measurement method of the depolarization [26,56].

[1] S. Castelletto, B. C. Johnson, V. Ivády, N. Stavrias, T. Umeda, A. Gali, and T. Ohshima, A silicon carbide room-temperature single-photon source, Nat. Mater. **13**, 151 (2014).

[2] I. Aharonovich, D. Englund, and M. Toth, Solid-state single-photon emitters, Nat. Photonics **10**, 631 (2016).

[3] T. M. Babinec, B. J. M. Hausmann, M. Khan, Y.-N. Zhang, J. R. Maze, P. R. Hemmer, and M. Lončar, A diamond nanowire single-photon source, Nat. Nanotechnol. **5**, 195 (2010).

[4] K. C. Miao, J. P. Blanton, C. P. Anderson, A. Bourassa, A. L. Crook, G. Wolfowicz, H. Abe, T. Ohshima, and D. D. Awschalom, Universal coherence protection in a solid-state spin qubit, Science **369**, 1493 (2020).

[5] J. R. Weber, W. F. Koehl, J. B. Varley, A. Janotti, B. B. Buckley, C. G. Van de Walle, and D. D. Awschalom, Quantum computing with defects, Proc. Natl. Acad. Sci. USA **107**, 8513 (2010).

[6] T. van der Sar, Z. H. Wang, M. S. Blok, H. Bernien, T. H. Taminiau, D. M. Toyli, D. A. Lidar, D. D. Awschalom, R. Hanson, and V. V. Dobrovitski, Decoherence-protected quantum gates for a hybrid solid-state spin register, Nature (London) **484**, 82 (2012).

[7] H. Bernien, B. Hensen, W. Pfaff, G. Koolstra, M. S. Blok, L. Robledo, T. H. Taminiau, M. Markham, D. J. Twitchen, L. Childress, and R. Hanson, Heralded entanglement between solid-state qubits separated by three metres, Nature (London) **497**, 86 (2013).

[8] W. S. Huxter, M. L. Palm, M. L. Davis, P. Welter, C.-H. Lambert, M. Trassin, and C. L. Degen, Scanning gradiometry with a single spin quantum magnetometer, Nat. Commun. **13**, 3761 (2022).

[9] Z.-W. Qiu, A. Hamo, U. Vool, T. X. Zhou, and A. Yacoby, Nanoscale electric field imaging with an ambient scanning quantum sensor microscope, npj Quantum Inf. **8**, 107 (2022).

[10] C. V. Raman and K. S. Krishnan, A new type of secondary radiation, Nature (London) **121**, 501 (1928).

[11] Z. Deutsch, L. Neeman, and D. Oron, Luminescence upconversion in colloidal double quantum dots, Nat. Nanotechnol. **8**, 649 (2013).

[12] H. M. Cheong, D. Kim, M. C. Hanna, and A. Mascarenhas, Effect of doping on photoluminescence upconversion in $GaAs/Al_xGa_{1-x}As$ heterostructures, Appl. Phys. Lett. **81**, 58 (2002).

[13] C. H. Camp Jr and M. T. Cicerone, Chemically sensitive bioimaging with coherent Raman scattering, Nat. Photon. **9**, 295 (2015).

[14] J. Zhang, D.-H. Li, R.-J. Chen, and Q.-H. Xiong, Laser cooling of a semiconductor by 40 kelvin, Nature (London) **493**, 504 (2013).

[15] D. V. Seletskiy, S. D. Melgaard, S. Bigotta, A. D. Lieto, M. Tonelli, and M. S.-Bahae, Laser cooling of solids to cryogenic temperatures, Nat. Photon. **4**, 161 (2010).

[16] R. I. Epstein, M. I. Buchwald, B. C. Edwards, T. R. Gosnell, and C. E. Mungan, Observation of laser-induced fluorescent cooling of a solid, Nature (London) **377**, 500 (1995).

[17] Q.-X. Wang, Q. Zhang, X.-X. Zhao, X. Luo, C. P.-Y. Wong, J.-Y. Wang, D.-Y. Wan, T. Venkatesan, S. J. Pennycook, K. P. Loh, G. Eda, and A. T. S. Wee, Photoluminescence upconversion by defects in hexagonal boron nitride, Nano Lett. **18**, 6898 (2018).

[18] Y.-F. Gao, Q.-H. Tan, X.-L. Liu, S.-L. Ren, Y.-J. Sun, D. Meng, Y.-J. Lu, P.-H. Tan, C.-X. Shan, and J. Zhang, Phonon-assisted photoluminescence up-conversion of silicon-vacancy centers in diamond, J. Phys. Chem. Lett. **9**, 6656 (2018).

[19] T. T. Tran, B. Regan, E. A. Ekimov, Z. Mu, Y. Zhou, W.-B. Gao, P. Narang, A. S. Solntsev, M. Toth, I. Aharonovich, and C. Bradac, Anti-Stokes excitation of solid-state quantum emitters for nanoscale thermometry, Sci. Adv. **5**, eaav9180 (2019).

[20] Y. Xu, H. Naramoto, K. Narumi, K. Miyashita, T. Kamiya, and T. Sakai, Strong anti-Stokes luminescence from H^+-irradiated diamond, Appl. Phys. Lett. **83**, 1968 (2003).

[21] J.-F. Wang, F.-F. Yan, Q. Li, Z.-H. Liu, J.-M. Cui, Z.-D. Liu, A. Gali, J.-S. Xu, C.-F. Li, and G.-C. Guo, Robust coherent control of solid-state spin qubits using anti-Stokes excitation, Nat. Commun. **12**, 3223 (2021).

[22] Y.-F. Gao, J.-M. Lai, Y.-J. Sun, X.-L. Liu, C.-N. Lin, P.-H. Tan, C.-X. Shan, and J. Zhang, Charge state manipulation of NV centers in diamond under phonon-assisted anti-stokes excitation of NV^0, ACS Photonics **9**, 1605 (2022).

[23] P. Siyushev, M. Nesladek, E. Bourgeois, M. Gulka, J. Hruby, T. Yamamoto, M. Trupke, T. Teraji, J. Isoya, and F. Jelezko, Photoelectrical imaging and coherent spin-state readout of single nitrogen-vacancy centers in diamond, Science **363**, 728 (2019).

[24] C. E. Weitzel, J. W. Palmour, C. H. Carter, K. Moore, K. K. Nordquist, S. Allen, C. Thero, and M. Bhatnagar, Silicon carbide high-power devices, IEEE Trans. Electron Devices **43**, 1732 (1996).

[25] V. A. Dmitriev, P. A. Ivanov, Ya. V. Morozenko, V. E. Chelnokov, and A. E. Cherenkov, Silicon carbide devices for active electronics and optoelectronics, Mater. Sci. Mono. **73**, 769 (1991).

[26] W. F. Koehl, B. B. Buckley, F. J. Heremans, G. Calusine, and D. D. Awschalom, Room temperature coherent control of defect spin qubits in silicon carbide, Nature (London) **479**, 84 (2011).

[27] R. Nagy, M. Niethammer, M. Widmann, Y.-C. Chen, P. Udvarhelyi, C. Bonato, J. U. Hassan, R. Karhu, I. G. Ivanov, N. T. Son, J. R. Maze, T. Ohshima, Ö. O. Soykal, Á. Gali, S.-Y. Lee, F. Kaiser, and J. Wrachtrup, High-fidelity spin and optical control of single silicon-vacancy centres in silicon carbide, Nat. Commun. **10**, 1954 (2019).

[28] J.-F. Wang, F.-F. Yan, Q. Li, Z.-H. Liu, H. Liu, G.-P. Guo, L.-P. Guo, X. Zhou, J.-M. Cui, J. Wang, Z.-Q. Zhou, X.-Y. Xu, J.-S. Xu, C.-F. Li, and G.-C. Guo, Coherent control of nitrogen-vacancy center spins in silicon carbide at room temperature, Phys. Rev. Lett. **124**, 223601 (2020).

[29] M. Zhao, S. A. Zargaleh, H. J. von Bardeleben, J. E. Fröch, M. Nonahal, H. B. Cai, X. G. Yang, J. Q. Yang, X. J. Li, I. Aharonovich, and W. B. Gao, Coherent manipulation with resonant excitation and single emitter creation of nitrogen vacancy centers in 4H silicon carbide, Nano Lett. **20**, 6142 (2020).

[30] F.-F. Yan, J.-F. Wang, Q. Li, Z.-D. Cheng, J.-M. Cui, W.-Z. Liu, J.-S. Xu, C.-F. Li, and G.-C. Guo, Coherent control of defect spins in silicon carbide above 550 K, Phys. Rev. Appl. **10**, 044042 (2018).

[31] L. Liu, J.-F. Wang, X.-D. Liu, H.-A. Xu, J.-M. Cui, Q. Li, J.-Y. Zhou, W.-X. Lin, Z.-X. He, W. Xu, Y. Wei, Z.-H. Liu, P. Wang, Z.-H. Hao, J.-F. Ding, H.-O. Li, W. Liu, H. Li, L.-X. You, J.-S. Xu *et al.*, Coherent control and magnetic detection of divacancy spins in silicon carbide at high pressures, Nano Lett. **22**, 9943 (2022).

[32] C. P. Anderson, E. O. Glen, C. Zeledon, A. Bourassa, Y. Jin, Y.-Z. Zhu, C. Vorwerk, A. L. Crook, H. Abe, J. U.- Hassan, T. Ohshima, N. T. Son, G. Galli, and D. D. Awschalom, Five-second coherence of a single spin with single-shot readout in silicon carbide, Sci. Adv. **8**, eabm5912 (2022).

[33] D. J. Christle, A. L. Falk, P. Andrich, P. V. Klimov, J. U. Hassan, N. T. Son, E. Janzén, T. Ohshima, and D. D. Awschalom, Isolated electron spins in silicon carbide with millisecond coherence times, Nat. Mater. **14**, 160 (2015).

[34] A. L. Falk, B. B. Buckley, G. Calusine, W. F. Koehl, V. V. Dobrovitski, A. Politi, C. A. Zorman, P. X.-L. Feng, and D. D. Awschalom, Polytype control of spin qubits in silicon carbide, Nat. Commun. **4**, 1819 (2013).

[35] F.-F. Yan, A.-L. Yi, J.-F. Wang, Q. Li, P. Yu, J.-X. Zhang, A. Gali, Y. Wang, J.-S. Xu, X. Ou, C.-F. Li, and G.-C. Guo, Room-temperature coherent control of implanted defect spins in silicon carbide, npj Quantum Inf. **6**, 38 (2020).

[36] Q. Li, J.-F. Wang, F.-F. Yan, J.-Y. Zhou, H.-F. Wang, H. Liu, L.-P. Guo, X. Zhou, A. Gali, Z.-H. Liu, Z.-Q. Wang, K. Sun, G.-P. Guo, J.-S. Tang, H. Li, L.-X. You, J.-S. Xu, C.-F. Li, and G.-C. Guo, Room temperature coherent manipulation of single-spin qubits in silicon carbide with a high readout contrast, Nat. Sci. Rev. **9**, nwab122 (2022).

[37] V. Nathan, A. H. Guenther, and S. S. Mitra, Review of multiphoton absorption in crystalline solids, J. Opt. Soc. Am. B **2**, 294 (1985).

[38] P. P. Paskov, P. O. Holtz, B. Monemar, J. M. Garcia, W. V. Schoenfeld, and P. M. Petroff, Photoluminescence up-conversion in InAs/GaAs self-assembled quantum dots, Appl. Phys. Lett. **77**, 812 (2000).

[39] N. S. Makarov, Q.-L. Lin, J. M. Pietryga, I. Robel, and V. I. Klimov, Auger up-conversion of low-intensity infrared light in engineered quantum dots, ACS Nano **10**, 10829 (2016).

[40] J. Binder, J. Howarth, F. Withers, M. R. Molas, T. Taniguchi, K. Watanabe, C. Faugeras, A. Wysmolek, M. Danovich, V. I. Fal'ko, A. K. Geim, K. S. Novoselov, M. Potemski, and A. Kozikov, Upconverted electroluminescence via Auger scattering of interlayer excitons in van der Waals heterostructures,xbrk Nat. Commun. **10**, 2335 (2019).

[41] W. Seidel, A. Titkov, J. P. André, P. Voisin, and M. Voos, High-efficiency energy up-conversion by an "auger fountain" at an InP-AlInAs type-II heterojunction, Phys. Rev. Lett. **73**, 2356 (1994).

[42] Y.-C. Dai, P.-F. Qi, G.-Y. Tao, G.-J. Yao, B.-B. Shi, Z.-X. Liu, Z.-C. Liu, X. He, P. Peng, Z.-B. Dang, L.-H. Zheng, T.-H. Zhang, Y.-J. Gong, Y. Guan, K.-H. Liu, and Z.-Y. Fang, Phonon-assisted upconversion in twisted two-dimensional semiconductors, Light Sci. Appl. **12**, 6 (2023).

[43] Z.-K. Ye, X. Lin, N. Wang, J.-H. Zhou, M.-Y. Zhu, H.-Y. Q., and X.-G. Peng, Phonon-assisted up-conversion photoluminescence of quantum dots, Nat. Commun. **12**, 4283 (2021).

[44] A. Lohrmann, B. C. Johnson, J. C. McCallum, and S. Castelletto, A review on single photon sources in silicon carbide, Rep. Prog. Phys. **80**, 034502 (2017).

[45] B. Magnusson, N. T. Son, A. Csóré, A. Gällström, T. Ohshima, A. Gali, and I. G. Ivanov, Excitation properties of the divacancy in 4*H*-SiC, Phys. Rev. B **98**, 195202 (2018).

[46] R. H. Brown and R. Q. Twiss, Correlation between Photons in two Coherent Beams of Light, Nature (London) **177**, 27 (1956).

[47] J. P. Hadden, J. P. Harrison, A. C. Stanley-Clarke, L. Marseglia, Y.-L. D. Ho, B. R. Patton, J. L. O'Brien, and J. G. Rarity, Strongly enhanced photon collection from diamond defect centers under microfabricated integrated solid immersion lenses, Appl. Phys. Lett. **97**, 241901 (2010).

[48] L. Orphal-Kobin, K. Unterguggenberger, T. Pregnolato, N. Kemf, M. Matalla, R.-S. Unger, I. Ostermay, G. Pieplow, and T. Schröder, Optically coherent nitrogen-vacancy defect centers in diamond nanostructures, Phys. Rev. X **13**, 011042 (2023).

[49] L. Z. Li, E. H. Chen, J. B. Zheng, S. L. Mouradian, F. Dolde, T. Schröder, S. Karaveli, M. L. Markham, D. J. Twitchen, and D. Englund, Efficient photon collection from a nitrogen vacancy center in a circular bullseye grating, Nano Lett. **15**, 1493 (2015).

[50] D. Le Sage, K. Arai, D. R. Glenn, S. J. DeVience, L. M. Pham, L. Rahn-Lee, M. D. Lukin, A. Yacoby, A. Komeili, and R. L. Walsworth, Optical magnetic imaging of living cells, Nature (London) **496**, 486 (2013).

[51] K. A. Ryu, C. M. Kaszuba, N. B. Bissonnette, R. C. Oslund, and O. O. Fadeyi, Interrogating biological systems using visible-light-powered catalysis, Nat. Rev. Chem. **5**, 322 (2021).

[52] C. Wang, H.-Q. Tao, L. Cheng, and Z. Liu, Near-infrared light induced in vivo photodynamic therapy of cancer based on upconversion nanoparticles, Biomaterials **32**, 6145 (2011).

[53] Y. T. Lim, S. Kim, A. Nakayama, N. E. Stott, M. G. Bawendi, and J. V. Frangioni, Selection of quantum dot wavelengths for biomedical assays and imaging, Mol. Imag. **2**, 50 (2003).

[54] S. Diao, G.-S. Hong, A. L. Antaris, J. L. Blackburn, K. Cheng, Z. Cheng, and H.-J. Dai, Biological imaging without autofluorescence in the second near-infrared region, Nano Res. **8**, 3027 (2015).

[55] A. L. Crook, Photonic enhancement of spin qubits in silicon carbide, Ph. D. dissertation, The University of Chicago 2021.

[56] W.-X. Lin, F.-F. Yan, Q. Li, J.-F. Wang, Z.-H. Hao, J.-Y. Zhou, H. Li, L.-X. You, J.-S. Xu, C.-F. Li, and G.-C. Guo, Temperature dependence of divacancy spin coherence in implanted silicon carbide, Phys. Rev. B **104**, 125305 (2021).